Petroleum Science 23 (2026) 7498–7510

Contents lists available at ScienceDirect

Petroleum Science

journal homepage: www.keaipublishing.com/en/journals/petroleum-science

Original Paper

Component-dependent transport and spatial distribution of crude oil fractions confined in kerogen nanopore

Shi-Deng Yuan [a], Ji-Chao Fang [b,*]

[a] School of Chemistry and Chemical Engineering, Qilu Normal University, Jinan, 250200, Shandong, China
[b] Petroleum Exploration and Production Research Institute, SINOPEC, Beijing, 102206, China

ARTICLE INFO

Article history:
Received 30 December 2025
Received in revised form
10 February 2026
Accepted 7 May 2026
Available online 13 May 2026

Edited by Min Li

Keywords:
Shale oil
Kerogen nanopore
Molecular dynamics simulation
Diffusion anisotropy
Interfacial adsorption

ABSTRACT

Understanding the transport mechanisms of shale oil in kerogen nanopores is critical for optimizing recovery from organic-rich reservoirs. Here, molecular dynamics simulations were employed to investigate the spatial distribution and diffusion behavior of various hydrocarbon fractions. Results revealed a distinct stratified distribution within the pores; asphaltenes and resins primarily occupied the interface region (7.49 nm in width), while light oil dominated the central phase (5.09 nm). Quantitatively, asphaltenes contributed 52.6% of the total contact with the kerogen matrix, significantly exceeding the 5.3% contribution from light oil. This intense interfacial interaction, characterized by π-π stacking and van der Waals forces, resulted in substantial mobility suppression, with asphaltene self-diffusion coefficients being the lowest among all fractions. Specifically, asphaltene motion was confined to localized thermal vibrations near pore walls, whereas light oil exhibited superior pore-axis diffusivity. A Quantitative Structure-Activity Relationship (QSAR) model developed via a Neural Network Algorithm effectively predicted these diffusion disparities ($R^2 = 0.95$), identifying molecular mass and electrostatic potential as governing descriptors. The wall adsorption-molecular aggregation dual mechanism elucidated here provides a molecular-scale rationale for the selective retention of heavy fractions and offers a theoretical framework for enhancing shale oil mobility through structural targeting.

© 2026 The Authors. Publishing services by Elsevier B.V. on behalf of KeAi Communications Co. Ltd. This is an open access article under the CC BY-NC-ND license (http://creativecommons.org/licenses/by-nc-nd/4.0/).

1. Introduction

The global paradigm shift toward unconventional energy resources has positioned shale oil as a pivotal component of the modern energy portfolio (Xu et al., 2022), necessitating a profound understanding of the complex fluid dynamics within organic-rich source rocks (Yang et al., 2017). Shale oil is predominantly sequestered within the nanoporous architecture of kerogen, a highly heterogeneous and disordered macromolecular organic matrix whose physicochemical properties differ fundamentally from those of conventional inorganic minerals (Bousige et al., 2016; Yu et al., 2020). Within these ultra-confined environments, the transport behavior of crude oil deviates significantly from bulk-phase hydrodynamics, as the characteristic pore dimensions often approach the molecular diameters of the constituent hydrocarbons (Liu and Zhang, 2019). Kerogen can retain up to 60% of shale oil, yet strong adsorption limits the mobility of this oil to less than 10%, severely restricting its recoverability (Gong et al., 2020; Perez and Devegowda, 2019; Sang et al., 2018; Zhang et al., 2025b; Zhu et al., 2020). Consequently, unraveling the microscopic mechanisms governing the spatial distribution and transport properties of multicomponent oil systems is essential for optimizing reservoir characterization and developing advanced enhanced oil recovery (EOR) strategies for unconventional play (Yang et al., 2025a; Zhan et al., 2024).

Crude oil trapped within kerogen is a complex mixture of diverse chemical species, typically classified into saturates, aromatics, resins, and asphaltenes (Wang et al., 2023; Yang et al., 2025b; Zhao et al., 2024). In the nanoconfined spaces of kerogen, the interaction between these fractions and the pore walls is governed by an intricate interplay of van der Waals forces, electrostatic interactions, and molecular-scale confinement effects, leading to pronounced competitive adsorption and selective transport phenomena (Fei et al., 2023). Despite the importance of these molecular-scale interactions, conventional reservoir

* Corresponding author.
E-mail address: fangjch.syky@sinopec.com (J.-C. Fang).
Peer review under the responsibility of China University of Petroleum (Beijing).

https://doi.org/10.1016/j.petsci.2026.05.007
1995-8226/© 2026 The Authors. Publishing services by Elsevier B.V. on behalf of KeAi Communications Co. Ltd. This is an open access article under the CC BY-NC-ND license (http://creativecommons.org/licenses/by-nc-nd/4.0/).

engineering models and continuum-based fluid mechanics often fail to account for the discrete nature of these components, resulting in significant inaccuracies when predicting the long-term production decline of shale reservoirs (Feng et al., 2020).

To bridge this knowledge gap, molecular dynamics (MD) simulations have emerged as a robust computational framework for probing the atomistic behavior of fluids under extreme confinement (Chen et al., 2023; Mehana et al., 2021; Xie et al., 2024). Fei et al. used MD simulations to elucidate the coupled adsorption-absorption behavior of shale oil in type II kerogen under varying reservoir conditions (Fei et al., 2023). Dawass et al. combined GCMC and molecular dynamics simulations to investigate how gas species distribute and migrate within a heterogeneous kerogen-clay composite nanopore system under high-pressure conditions (Dawass et al., 2023). Recent studies demonstrate that oil components are not only adsorbed onto kerogen surfaces but also absorbed into aliphatic matrix spaces, a process highly sensitive to temperature and aqueous conditions (Fei et al., 2023). Within these confined environments, n-alkanes undergo significant shifts in vapor-liquid equilibrium, where longer-chain molecules show greater adaptability to confinement-induced effects (Li et al., 2025). Interfacial mechanisms, governed by van der Waals and electrostatic interactions, lead to the preferential adsorption of polar species, which subsequently dictates divergent transport patterns (Zhang and Lu, 2025). Furthermore, molecular-scale displacement studies reveal that competitive adsorption is critical for mobilizing these components. For instance, CO_2 exhibits higher recovery potential than N_2 or water by effectively disrupting adsorbed oil layers and asphaltene aggregates (Zhang et al., 2025b). Despite recent advances in this hybrid methodology, the specific impact of heavy components like resins and asphaltenes on the overall diffusion kinetics within kerogen pores remains inadequately understood, particularly regarding how their structural features contribute to the overall resistance to flow.

In this work, a systematic investigation into the flow behavior of multicomponent oil systems within kerogen nanopores was presented by combining multiscale MD simulations with data-driven machine learning (ML) modeling. We first evaluate the differential distribution and kinetic characteristics of light oil, resins, and asphaltenes, providing a quantitative assessment of how heavy fractions influence the mobility of the overall oil phase through the formation of stagnant layers and molecular clustering. Subsequently, we construct a comprehensive ML framework to evaluate the sensitivity of diffusion coefficients to a diverse set of molecular features, aiming to establish a generalized predictive model for hydrocarbon transport in organic nanopores. The results of this work not only offer a molecular-level explanation for the fractionation effects observed during shale oil extraction but also provide a powerful computational tool for the rapid assessment of fluid transport in complex, unconventional geological systems.

2. Methods

2.1. Model of kerogen nanopore

Organic-rich shale formations are characterized by an extensive network of carbonaceous nanopores, which function as the primary conduits for both the storage and migration of hydrocarbon fluids. Within this organic framework, kerogen stands as the defining constituent, manifesting in various geochemical classifications depending on its origin and thermal maturity (Gao et al., 2020; Lin et al., 2023). For the present investigation, the molecular architecture of type II-C kerogen was adopted, following the foundational structural derivations established by previous works (Ungerer et al., 2015; Zhang and Lu, 2025). This specific high-

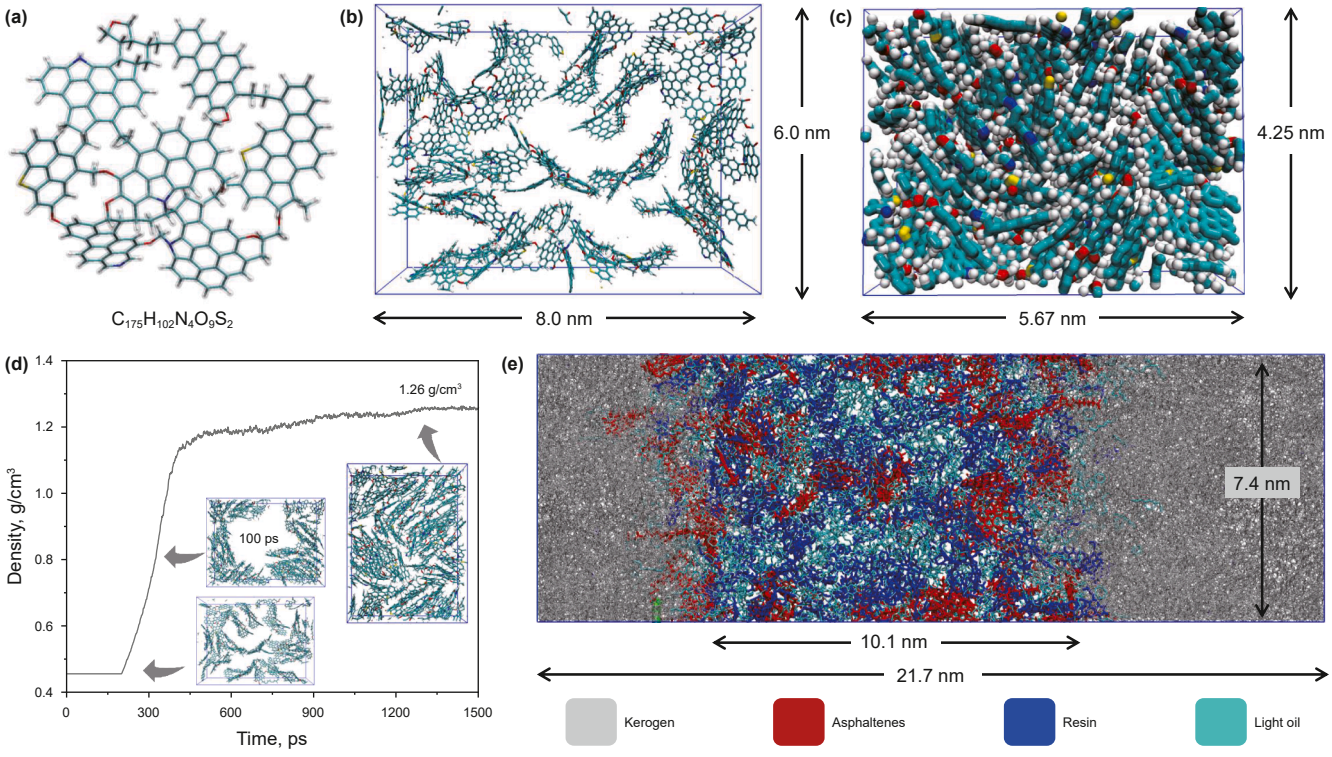


Fig. 1. Model building. **(a)** Molecular model of type II-C kerogen, **(b)** initial configuration obtained from simulated annealing of kerogen molecules, **(c)** equilibrated kerogen surface structure following annealing, **(d)** evolution of kerogen density throughout the annealing process, **(e)** model of oil droplets of different compositions within kerogen nanopore.

maturity variant, represented by the chemical formula $C_{242}H_{219}O_{13}N_5S_2$ (as shown in Fig. 1(a)), has gained widespread recognition in the literature as a benchmark for evaluating the adsorptive characteristics, phase behavior, and transport dynamics of shale oil under diverse reservoir conditions (Yang et al., 2020). To construct a representative organic nanopore environment, an ensemble of 16 kerogen macromolecular units was integrated into a primary simulation cell with spatial dimensions (8 nm × 6 nm × 3 nm in Fig. 1(b)). To resolve potential atomic clashes and eliminate unphysical van der Waals overlaps, the initial configuration underwent a rigorous energy minimization protocol utilizing the conjugate gradient algorithm.

To replicate the intricate organic pore structures characteristic of subsurface geological environments, an initial thermal stabilization of 16 kerogen macromolecular units was conducted within the canonical ensemble. During this phase, the system was subjected to a sustained temperature of 900 K for a 5 ns duration, facilitating the spontaneous aggregation of individual molecules into a cohesive, centralized cluster. To further refine the structural integrity and mimic the long-term geochemical maturation process, this condensed block was subjected to a rigorous multi-stage annealing protocol under the isobaric-isosteric (NPT) ensemble (Zhang and Lu, 2025). This controlled cooling and compression sequence allowed the organic matrix to achieve a realistic surface morphology and internal porosity consistent with deep-earth conditions. The equilibrated kerogen surface structure following annealing was shown in Fig. 1(c). The corresponding evolution of the kerogen density was depicted quantitatively in Fig. 1(d). The simulated density profiles exhibit strong congruence with established experimental benchmarks, wherein laboratory-derived measurements for kerogen matrices under analogous structural and thermobaric conditions typically fall within the 1.18 to 1.35 g/cm^3 interval (Okiongbo et al., 2005). This close agreement with empirical literature values serves as a robust validation of the atomistic model's fidelity and the reliability of the equilibrium configurations. To construct the confined pore geometries, the kerogen matrix segments presented in Fig. 1(c) were subjected to a 180° rotation about the longitudinal *z*-axis, thereby creating a symmetrical slit-pore architecture with tunable apertures. Subsequently, a heterogeneous population of oil model was introduced into the interstitial void space. This integration process culminated in the establishment of the comprehensive simulation domain, as visualized in the composite model in Fig. 1(e).

2.2. Oil model

The synthesis of representative hydrocarbon aggregates from structurally heterogeneous species is fundamental to deciphering the relationship between molecular architecture and the subsequent spatial partitioning and transport kinetics within the kerogen matrix. In the present study, a high-fidelity heavy crude oil surrogate was engineered through the stochastic distribution of a diverse molecular ensemble. This mixture comprised a stratified composition of two asphaltenes and six resin variants interspersed with a broad spectrum of light fractions (Yuan et al. 2025a, 2026a, 2026b). The paraffinic and aromatic constituents included a series of linear alkanes (C6 through C9), alongside cyclic and alkyl-substituted hydrocarbons such as cycloheptane, cyclohexane, benzene, and toluene. By integrating these specific SARA-based components, the model captures the intrinsic competitive interactions and steric effects governing fluid behavior in organic nanostructures. Previous experimental studies consistently show that kerogen-hosted pores are predominantly nanoporous, with characteristic diameters mainly distributed below 10 nm (Clarkson et al., 2013; Ross and Marc Bustin, 2009). Therefore, oil molecules were then randomly inserted into the kerogen pores with a diameter of 10 nm (as shown in Fig. 1(e)). Finally, the system included 256 kerogen, 279 hexane, 230 heptane, 306 octane, 355 nonane, 184 cyclohexane, 306 cycloheptane, 108 benzene, 296 toluene, 63 resin 1, 41 resin 2, 55 resin 3, 54 resin 4, 41 resin 5, 49 resin 6, 36 asphaltene 1, and 32 asphaltene 2 molecules. The structures of two asphaltenes and six resin molecules were presented in Fig. S1.

2.3. QSAR modeling

The Quantitative Structure-Activity Relationship (QSAR) paradigm represents a robust machine learning framework, widely utilized for the prognostic modeling and characterization of molecular behaviors in complex environmental systems (Yuan et al. 2024b, 2025b). In this study, a multifaceted ensemble of 17 molecular descriptors (detailed in Table S1) was systematically curated to elucidate the intrinsic connection between the diffusion behavior of oil molecules in kerogen nanopores and their intrinsic molecular attributes. This descriptor suite encompasses 3 constitutional parameters (*NA*, *M*, *V*), 14 quantum chemical descriptors (σ^2_{tot}, μ, MPI, $\overline{V}_S^-$, $\overline{V}_S^+$, A^-, A^+, $|\Theta|$, $V_{S,max}$, $V_{S,min}$, A_{non}, E_{HOMO}, E_{LUMO}, ΔE_{gap}). An independent validation set following a 3:1 ratio (75% and 25%, respectively). These electronic and structural features were derived through high-level quantum mechanical calculations performed at the M06-2X/def2TZVP theoretical level using the Multiwfn (Lu and Chen, 2012) code. The predictive architecture was subsequently finalized through a rigorous hierarchical workflow, integrating collinearity assessment, genetic function approximation (GFA), and neural network analysis (NNA) followed by comprehensive statistical validation to ensure model generalizability.

2.4. Simulations set-up

The force field parameters for all molecular species were derived using the GROMOS 54a7 force field, with topologies generated through the Automated Topology Builder (ATB) repository to ensure chemical consistency. Regarding the force field selection, the GROMOS force field was employed primarily due to its superior performance in characterizing the transport kinetics and self-diffusion coefficients of condensed-phase organic fluids, especially in kerogen-oil systems (Bui et al., 2020; Michalec and Lísal, 2017; Zhan et al., 2024). The production phase involved a 100 ns trajectory propagated within the isothermal-isobaric (NPT) ensemble via Gromacs software. Three-dimensional periodic boundary conditions (PBC) were implemented across all Cartesian axes, utilizing an integration time step of 1 fs. Systematic pressure control was maintained at 30 MPa via the Berendsen barostat with a coupling constant of 1.0 ps, while the system temperature was stabilized at 365.15 K through the velocity-rescaling (v-rescale) thermostat. The simulation temperature (365.15 K) and pressure (30 MPa) reflect typical mid-to-deep reservoir conditions (Chiang et al., 2020; Nadeau et al., 2023), ensuring realistic oil-kerogen interactions and consistency with established benchmarks in prior MD literature (Fei et al., 2023; Wu et al., 2022; Zhang and Lu, 2025). Long-range electrostatic interactions were accurately resolved using the Particle Mesh Ewald (PME) summation technique. A cutoff radius of 1.4 nm was employed for the non-bonded interactions. Post-simulation analysis and structural rendering were conducted using the Visual Molecular Dynamics (VMD 1.9.4) software package. The pressure control via the NPT ensemble was

applied to the entire simulation system, including both the kerogen matrix and the confined fluid phase.

3. Results and discussion

3.1. Interaction between kerogen

Elucidating intermolecular interactions among kerogen units was essential for understanding the formation of organic nanopores and their controlling role in hydrocarbon storage and transport at the molecular scale (Li et al., 2025). Therefore, the interaction between kerogen molecules were investigated in this section. The equilibrated configuration of the kerogen-oil system, as illustrated in the cross-sectional snapshot in Fig. 2(a), revealed a highly disordered and heterogeneous organic matrix that more faithfully replicates the chaotic nature of native shale environments. Unlike conventional modeling approaches (Michalec and Lísal, 2017) that simplify the kerogen architecture into pre-aligned, uniformly layered domains, our packing procedure employs a stochastic insertion of kerogen macromolecular units. This randomized orientation facilitates the formation of tortuous, non-uniform nanopore geometries, effectively capturing the structural anisotropy and variegated functional group exposure inherent in real geochemical matrices.

Fig. 2(a) illustrated the primary interaction modes between kerogen molecules, which were predominantly governed by π-π stacking. Consequently, the interaction cross-sections exhibited quasi-lattice-like alignment features, reflecting the ordered self-assembly behavior induced by the stacking of aromatic architectures. The localized magnification in Fig. 2(b) further substantiated this π-π stacking modality, clearly demonstrating the face-to-face close-packing characteristics of aromatic moieties within the kerogen matrix. The emergence of this interaction pattern originated from the abundance of aromatic and heterocyclic functional groups within the kerogen molecules, including 2,3,4,5-tetrahydropyridine (2,3,4,5-THPYR), pyrrole (PPY), N-substituted alkylpiperidines (N-APIP), tetrahydrofuran (THF), hydroxyl-containing single-bond structures, and thiophene (THIOP). These groups were rich in aromatic ring systems and possessed low molecular planarity parameters (approximately 0.3) (Wang et al., 2025), which facilitated effective orbital overlap and fulfilled the geometric requirements for the formation of π-π stacking interactions (Grimme, 2008). Under the spatial confinement of dense kerogen nanopores, these structural attributes significantly intensified the π-π stacking effects, leading to the development of robust molecular cohesion and localized ordered domains within the organic matrix.

Fig. 2(c) provided a quantitative characterization of the inter-molecular interaction energy between individual kerogen units, calculated as the total interaction energy of the ensemble normalized by the number of kerogen molecules. To determine specific inter-group energies, “energygrps” were defined in the *mdp* file, and existing trajectories were processed via the *gmx rerun* utility using the original force field parameters. The results indicated that the inter-molecular interactions were primarily dominated by van der Waals (vdW) interaction (−831.8 kJ/mol, about 69.1%), whereas electrostatic contributions remained relatively secondary (−363.6 kJ/mol, about 36.9%). This disparity suggested that non-bonded weak interactions played a definitive role in governing the self-assembly process of the kerogen matrix. To further elucidate the physical underpinnings of this phenomenon, the Independent Gradient Model based on Hirshfeld partitioning (IGMH) was employed to visualize the inter-molecular vdW interactions via Multiwfn code (Lu, 2024; Lu and Chen, 2012, 2022). The representative configuration of the kerogen dimer was initially extracted from the stable production trajectory of MD simulation. The ORCA 5.0 software package was employed to perform further geometry optimization and wavefunction

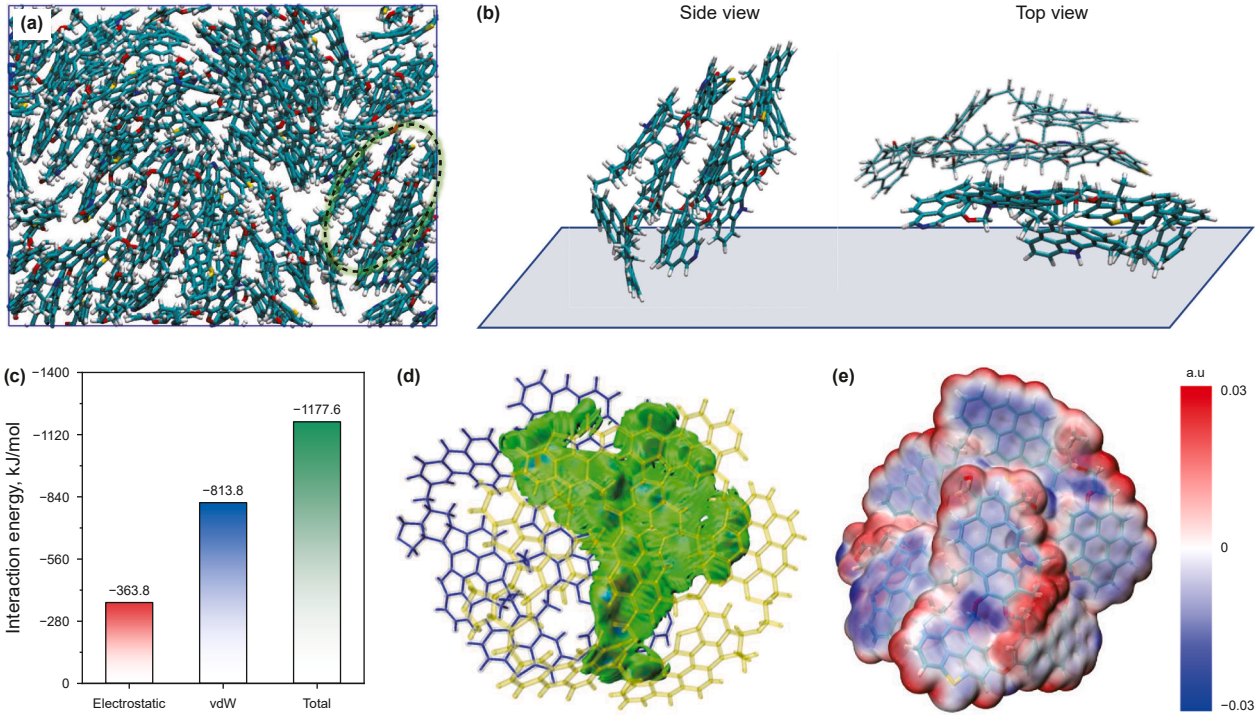


Fig. 2. **(a)** Snapshot of the overall arrangement of kerogen molecules and **(b)** enlarged view of a local region. **(c)** Intermolecular interaction energies among kerogen molecules. **(d)** Visualization of van der Waals interactions between kerogen molecules, where the green regions indicate van der Waals interaction domains. **(e)** Electrostatic potential distribution on the kerogen molecular surface, with red and blue regions representing positive and negative electrostatic potential, respectively.

calculation (Neese, 2022; Stephens et al., 1994). As illustrated in Fig. 2(d), a broad and continuous distribution of vdW interaction domains emerged as the kerogen molecules engaged in π-π stacking, which significantly amplified the inter-molecular attractive intensity. This extensive interaction region originated from the superior spatial complementarity and orbital overlap inherent to the aromatic ring systems. Furthermore, the molecular surfaces of the kerogen units exhibited large-area distributions of both positive and negative electrostatic potential (ESP in Fig. 2(e) and Fig. S2) regions (Zhang and Lu, 2021). Upon molecular approach, the spatial overlap of these oppositely charged ESP domains contributed to a localized enhancement of the electrostatic interaction. Although its overall contribution was subordinate to the vdW interaction, the electrostatic interaction nonetheless exerted a supplementary regulatory effect on the localized structural stability and the directional orientation of molecular alignment.

In summary, the robust π-π stacking and vdW-dominated cohesion within the kerogen matrix establish a chemically heterogeneous template that defines the fundamental energetic landscape of the organic nanopores. These architectural features, characterized by dense aromatic clusters and nuanced ESP distributions, are expected to serve as the primary determinants for the selective sequestration and interfacial resistance encountered by the infiltrating hydrocarbon phases. Building upon this established structural and energetic foundation, the following section examines how the varying affinities of asphaltenes, resins, and light oil for the kerogen surface translate into distinct spatial distributions. And determine the macroscopic transport efficiency within the shale matrix.

3.2. Equilibrium distribution of shale oil

The equilibrium adsorption snapshots presented in Fig. 3(a) revealed a distinct stratified distribution of shale oil fractions within the kerogen nanopores, where red-colored asphaltenes were sequestered adjacent to the pore walls, followed by blue-colored resins, while cyan light oil molecules predominantly occupied the central channel. This spatial heterogeneity reflected the competitive adsorption disparities among the oil phase constituents at the molecular scale (Zhang and Lu, 2025). Asphaltene molecules (Schuler et al., 2020), owing to their high molecular weight, aromatic complexity, and heteroatom content, interacted most strongly with kerogen, leading to the highest surface affinity. Resins, which possessed intermediate structural complexity and polarity bridging asphaltenes and light oil, featured both aromatic motifs capable of stacking and flexible aliphatic chains, resulting in moderate adsorptive capacities and their consequent spatial positioning between the adsorbed layer and the bulk phase. In contrast, the light oil molecules, characterized by lower molecular weights, simplified topologies, and weaker polarity, demonstrated limited interactions with the kerogen substrate. Consequently,

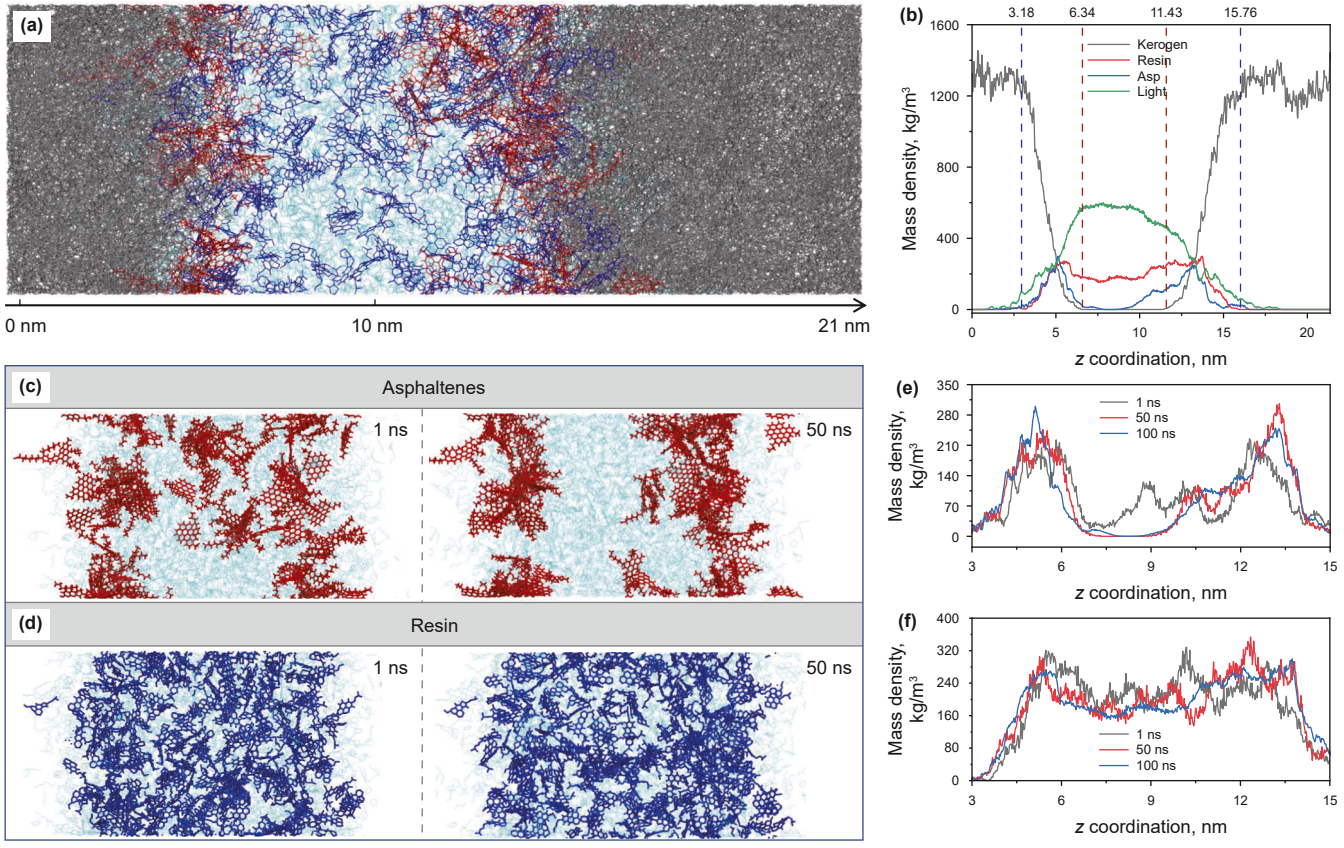


Fig. 3. **(a)** Snapshot of shale oil distribution in the system after equilibration, where gray, red, blue, and cyan represent kerogen, asphaltenes, resins, and light oil components, respectively. **(b)** Mass density profiles of shale oil components and kerogen averaged over the final 2 ns of the simulation. Diffusion snapshots of shale oil components during the simulation for **(c)** asphaltenes and **(d)** resins. Temporal evolution of mass density distributions for different components for **(e)** asphaltenes and **(f)** resins.

light oil tended to partition away from the pore walls toward the central bulk region, exhibiting superior mobility. The qualitative observations of molecular stratification were further corroborated by the quantitative mass density profiles presented in Fig. 3(b). The bulk density of the kerogen matrix stabilized at approximately 1250 kg/m^3, a value consistent with established literature (Okiongbo et al., 2005), thereby validating the accuracy of the applied force field parameters and the environmental configuration of the simulation. In addition, the interaction energy calculations reveal that light oil exhibits the strongest affinity to the kerogen pore (Fig. S3), followed by resins and asphaltenes. This energetic trend is consistent with their spatial distribution in kerogen nanopores, with stronger interactions leading to higher accumulation near the pore surface (Fig. 3(b)).

Based on the spatial variation of the kerogen density, the simulation domain was rigorously demarcated into three distinct zones: the kerogen phase, where the density remained constant; the interface region, characterized by a gradual density gradient spanning a substantial width of 7.49 nm; and the oil phase, defined by the complete absence of kerogen and covering a span of 5.09 nm. Within these defined regions, the asphaltene molecules exhibited a characteristic bimodal distribution concentrated exclusively within the upper and lower interface regions, with negligible presence detected in either the bulk oil or the solid kerogen phases. Conversely, the light oil and resin fractions displayed a broader spatial occupancy, extending across both the bulk oil phase and the interfacial transition zones. Fig. 3(c)–(f) further illustrated the interfacial diffusion tendency of asphaltene and resin molecules. These quantitative findings suggested that the substantial entrapment of hydrocarbon components within the spatially extensive interface region constituted the fundamental physical barrier impeding efficient shale oil recovery (Chen et al., 2026).

3.3. Oil diffusion within kerogen nanopore

Building upon the aforementioned spatial demarcation of the kerogen nanopore, the specific distribution characteristics of each oil phase component across these distinct regions were systematically evaluated. As illustrated in the quantitative proportion analysis in Fig. 4(a) and the corresponding three-dimensional visualization in Fig. S4, the kerogen phase was predominantly occupied by light oil molecules, which constituted approximately 67.3% of the total composition. This predominance was primarily attributed to the non-polar nature, compact molecular dimensions, and superior diffusivity of the light alkane species, which facilitated their deep penetration and extensive dispersion within the dense organic matrix. Despite their substantial steric bulk, asphaltenes maintained a significant presence (26.6%) within the kerogen phase, indicating that strong intermolecular interactions with the kerogen skeleton effectively overcame steric hindrance to promote retention. In contrast, resins accounted for only 6.1% of the population, suggesting that their specific structural and polar attributes were insufficient to sustain stable accumulation within the organic framework. In the interfacial region, the distribution of asphaltenes, resins, and light crude oil molecules was relatively balanced (Fig. 4(b) and Fig. S5), at 23.5%, 32.1%, and 44.4%, respectively. Specifically, the aromatic cores and polar functional groups of asphaltenes and resins favored their enrichment at the kerogen-oil boundary, thereby mitigating the compositional disparities observed elsewhere. Conversely, the bulk oil phase was dominated by the smaller, highly mobile resin (27.2%) and light oil (68.8%)

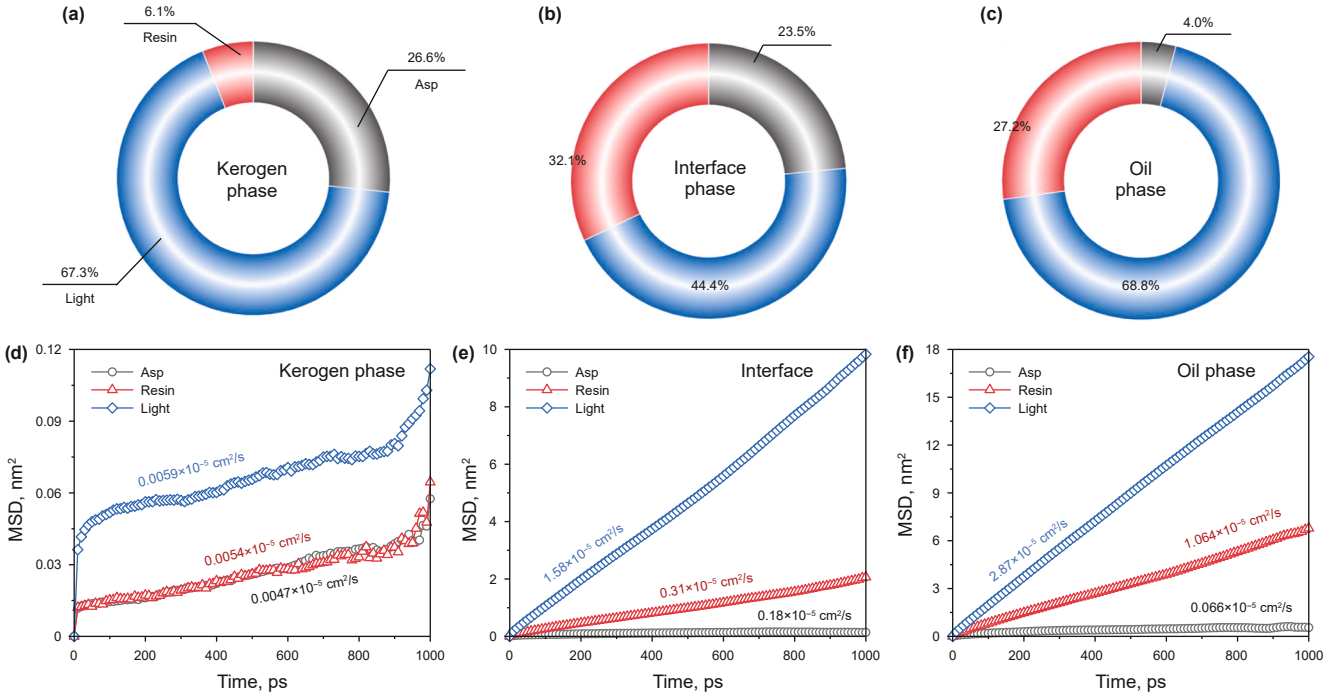


Fig. 4. Proportional distribution of asphaltene, resin, and light oil molecules across different regions of the kerogen pore for **(a)** the kerogen phase, **(b)** the interfacial region, and **(c)** the oil phase. Corresponding diffusion coefficients of asphaltene, resin, and light oil molecules in different pore regions for **(d)** the kerogen phase, **(e)** the interfacial region, and **(f)** the oil phase.

fractions, whereas asphaltenes represented a mere 4.0% in Fig. 4(c). This sharp decline confirmed that the large molecular volume and restricted diffusivity of asphaltenes confined them primarily to the pore walls and interfacial zones, preventing their effective release into the free oil continuum.

The mean square displacement (MSD) and diffusion coefficient (D) for the crude oil phase were further calculated in Fig. 4(d)–(f) by the following equation (Allen and Tildesley, 1987):

$$\mathrm{MSD}(t) = \langle \frac{1}{N_a} \sum_{i=1}^{N_a} |r_i(t) - r_i(0)|^2 \rangle \quad (1)$$

$$D_a = \frac{1}{2dN_a} \lim_{t\to\infty} \frac{d}{dt} \sum_{i=1}^{N_a} \langle [r_i(t) - r_i(0)]^2 \rangle \quad (2)$$

where N_a denotes the number of atoms, while $r_i(t)$ and $r_i(0)$ represent the positions of the i atom at time t and time 0, respectively, with d representing the system dimension. While oil components within the interfacial layers exhibit sub-diffusive behavior due to potent adsorption potentials, the Einstein relation is employed to derive D as a robust comparative metric for molecular mobility (Zhang and Lu, 2025; Zhang et al., 2025a; Zhao et al., 2025). This methodology aligns with established protocols in nanoporous systems, where the linear regime of regional MSD curves serves as a quantitative proxy for the penetrability and escape probability of guest molecules. By establishing a quantitative hierarchy of mobility across different oil fractions, this approach effectively correlates the trapping effect of kerogen's aromatic clusters with transport kinetics, providing a consistent baseline for bridging microscopic structural descriptors with macroscopic transport properties.

Although the self-diffusion coefficient of light oil within the kerogen phase was significantly higher than those of asphaltenes and resins, it remained remarkably low at only 5.9×10^{-7} cm^2/s in Fig. 4(d). This result indicated that the overall mobility of all oil components was severely restricted by the synergy of intense spatial confinement and pronounced molecule-matrix interactions, hindering their effective migration and ultimate recovery from the kerogen framework (Vasileiadis et al., 2018). In the interfacial region, the diffusion coefficients of the various oil phase components exhibited a distinct hierarchical characteristic (Fig. 4(e)), following the order: asphaltenes (0.18×10^{-5} cm^2/s) < resins (0.31×10^{-5} cm^2/s) < light oil (1.58×10^{-5} cm^2/s). Asphaltenes exhibited the most significant mobility suppression due to their high molecular weight, pronounced aromaticity, and propensity for π-π stacking and van der Waals interactions with the kerogen matrix. Resins, possessing intermediate structural complexity and polarity, displayed moderate diffusivity (as shown in Fig. S6). In contrast, light oil molecules, characterized by simplified architectures and weaker polarity, experienced the least confinement within the interface regions, resulting in higher diffusion coefficients. Within the bulk oil phase, the relative hierarchy of diffusion coefficients across all components remained consistent (Fig. 4(f)), further demonstrating that intrinsic molecular structural features exerted a dominant influence on transport behavior. In this context, the regional environment primarily modulated the absolute diffusion magnitudes by regulating the intensity of molecule-wall interactions.

Within the kerogen nanopores, the transport of oil molecules was decoupled into two primary modes: pore-axis diffusion and cross-pore diffusion, as illustrated in Fig. 5(a). Given that the migration and displacement processes of shale oil within the reservoir predominantly occur along the pore axis, this section focused on evaluating the distinct characteristics of these two

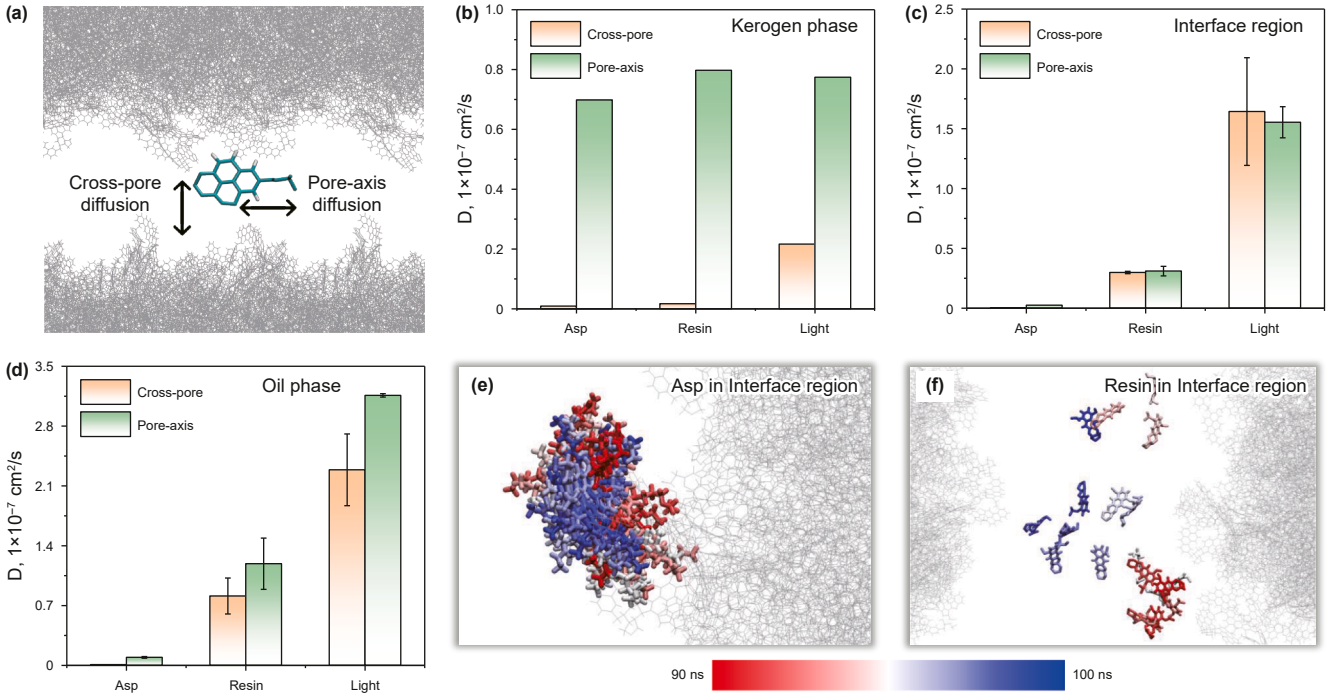


Fig. 5. **(a)** Schematic illustration of oil molecule diffusion along the pore axis (pore-axis diffusion) and perpendicular to the pore (cross-pore diffusion) direction within a kerogen nanopore. Diffusion coefficients of different oil components along and perpendicular to the pore direction in **(b)** the kerogen phase, **(c)** the interfacial region, and **(d)** the oil phase. **(e)** Time-resolved superimposed diffusion trajectories of asphaltene and resin molecules over the final 10 ns of the simulation.

diffusion behaviors within the kerogen matrix. As shown in Fig. 5(b), the cross-pore diffusion coefficients of oil molecules within the kerogen phase were significantly lower than their pore-axis counterparts, indicating that hydrocarbon migration within the kerogen nanopores was predominantly governed by axial diffusion. This pronounced diffusion anisotropy originated primarily from the geometric confinement of the nanopore architecture and the stringent constraints imposed by the pore walls on lateral molecular displacement. In the interface region, the diffusion behavior exhibited heightened sensitivity to the molecular structures of the oil components, whereas the disparity between pore-axis and cross-pore diffusion coefficients was significantly attenuated (Fig. 5(c)). This reduction in anisotropy was likely attributable to the competitive influence of the kerogen adsorption potential field and the intermolecular interactions among the oil phase constituents. Such a combined energetic environment allowed the molecules to retain a degree of lateral mobility while remaining near the pore walls, thereby weakening the directional constraints on diffusion. Within the bulk oil phase (Fig. 5(d)), the diffusion coefficients reverted to a state where pore-axis diffusion exceeded cross-pore diffusion, indicating that the pore geometry continued to exert a regulatory influence on the directionality of molecular transport even in the absence of immediate wall constraints. However, the degree of restriction was significantly attenuated compared to that observed within the kerogen phase. Fig. 5(e) provided a visual verification of the diffusion behaviors from a configurational trajectory perspective at last 10 ns. It was observed that the asphaltene molecules remained predominantly confined to the vicinity of the kerogen pore surfaces, with their motion characterized primarily by localized thermal vibrations rather than long-range migration. Conversely, the resin molecules demonstrated the capacity to progressively detach from the interfacial adsorption zones and diffuse toward the bulk oil phase within the pore center, thereby exhibiting superior mobility. Overall, the various oil phase components exhibited significant diffusion anisotropy within the kerogen nanopores, with their transport modalities being synergistically controlled by the intensity of molecule-matrix interactions, and the intrinsic structural characteristics of the molecules themselves.

Given that the interaction between oil molecules and the kerogen pore walls exerts a decisive influence on fluid mobility, this section further quantitatively analyzed the dynamic contact behavior of different oil components within the kerogen nanopores. An interaction was defined as an effective contact when the distance between an oil molecule and a kerogen atom fell below 0.6 nm. To highlight the temporal evolution of this behavior, the contact counts for all oil components were initialized to zero at the onset of the simulation. The incremental contact counts recorded during the simulation were illustrated in Fig. 6(a). It was observed that the number of contacts between the kerogen matrix and various oil components increases sharply at the initial stage and gradually reaches a plateau after approximately 80 ns, indicating that the system has attained equilibrium. Besides, the asphaltene molecules consistently exhibited the highest frequency of contacts

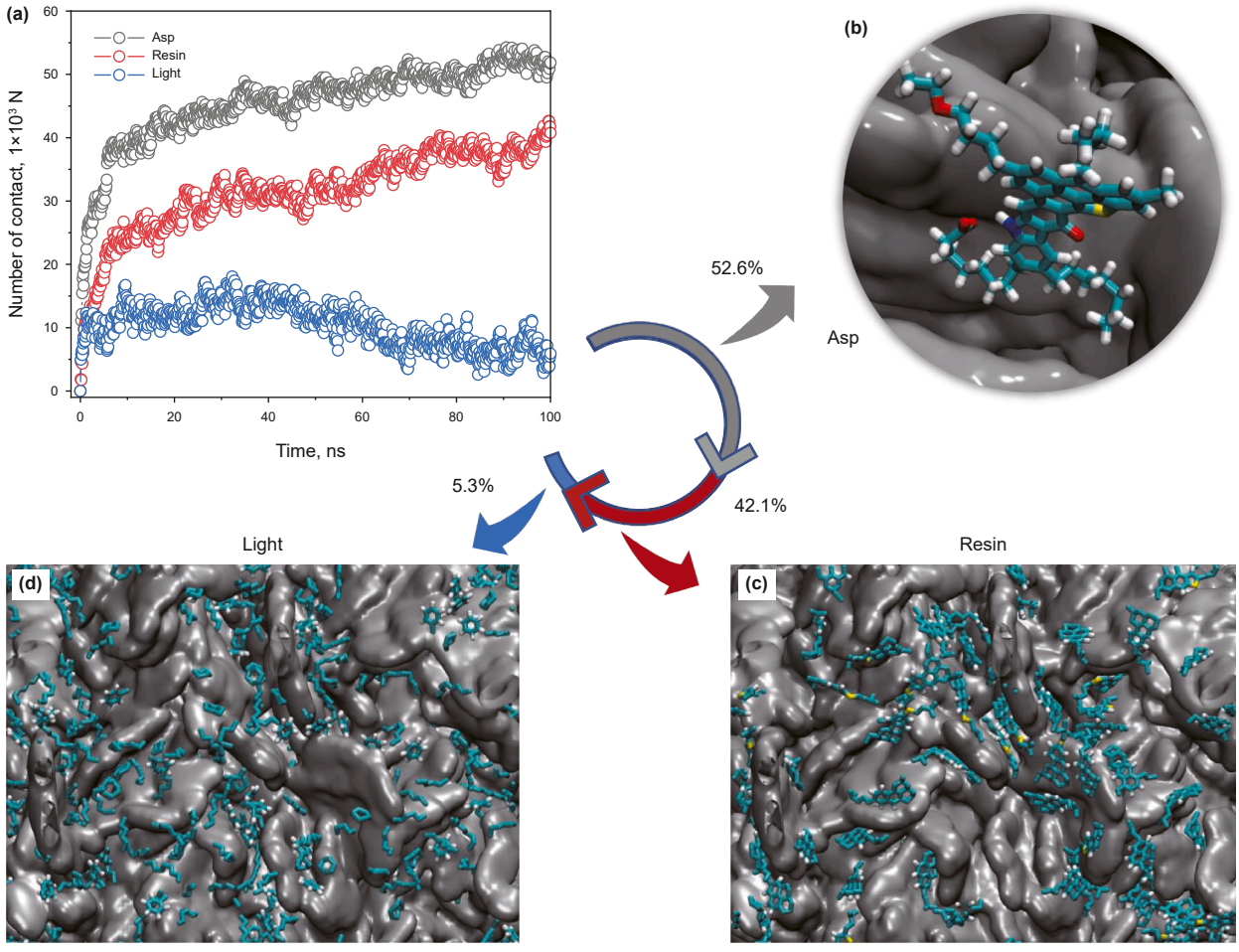


Fig. 6. **(a)** Time evolution of the number of contacts between kerogen and different oil components. Representative snapshots illustrating interactions between the kerogen surface and **(b)** asphaltene, **(c)** resin, and **(d)** light oil molecules.

with the kerogen matrix, followed by resins, whereas light oil molecules displayed the fewest interactions. This trend was highly consistent with the spatial distribution and diffusion characteristics previously observed, reflecting the dominant role of molecular structural complexity and intermolecular interaction strength in governing interfacial adsorption behavior.

The relative contributions of each component to the total kerogen contact number were further calculated, as presented in Fig. 6(b)–(d). The results indicated that asphaltenes accounted for a substantial 52.6% of the total contacts, followed by resins at 42.1%, while light oil molecules contributed a mere 5.3%. This disparity suggested that asphaltene and resin molecules established a more stable and persistent interaction network in the vicinity of the pore walls, which significantly intensified interfacial retention effects and consequently suppressed their mobility. In contrast, the minimal contact frequency of light oil molecules resulted in significantly attenuated interfacial confinement; consequently, these molecules demonstrated the highest diffusion coefficients within the kerogen pores, exhibiting a distinct advantage in pore-axis diffusion. Although their cross-pore diffusion remained restricted by geometric confinement, their overall degree of migratory freedom was significantly superior to that of the asphaltene and resin fractions.

Beyond the confinement imposed by the kerogen pore walls, the mobility of asphaltene molecules was further attenuated by multiple interactions with surrounding oil phase constituents, resulting in significantly restricted diffusion behaviors. As illustrated in Fig. 7(a), the interaction network involving asphaltenes encompassed not only the kerogen matrix but also fellow asphaltenes, resins, and light oil molecules within the oil phase. Notably, due to their structural complexity and pronounced aromaticity, the asphaltenes and resins within the oil phase were more prone to establishing effective contacts and forming stable molecular aggregates with the target asphaltene molecules. RDF analysis further elucidated this molecular-scale aggregation mechanism. As depicted in Fig. 7(b), the asphaltene–asphaltene RDF exhibited a distinct primary peak at approximately 0.35 nm and a secondary peak at roughly 0.70 nm. These peaks corresponded to the face-to-face stacking and offset stacking configurations of aromatic rings (Cui et al., 2026), respectively, indicating a strong propensity for self-aggregation among asphaltene molecules. In comparison, the peak intensity of the asphaltene-resin RDF was generally lower than that of the asphaltene-asphaltene system, suggesting a relatively weaker interaction strength. However, a degree of synergistic stacking persisted, as visually corroborated by the structural snapshot in Fig. 7(c). The quantitative evaluation of interaction energies provided further corroboration for these findings (Fig. 7(d)). Calculated on a per-molecule basis (total energy divide by 68 asphaltene molecules), the interaction energy between a target asphaltene and surrounding asphaltene molecules was the most substantial, reaching −374.6 kJ/mol. Conversely, the interaction energies between asphaltenes and resins, light oil, or kerogen were comparable, averaging approximately −105.5 kJ/mol. Although weaker than asphaltene self-aggregation, these interactions remained non-negligible within the confined pore environment. Collectively, asphaltene molecules were subjected to strong adsorption and spatial confinement by the kerogen pore walls, while simultaneously engaging in significant self-aggregation and synergistic interactions with heavy components like resins to form highly stable localized structural networks. This dual mechanism of "wall adsorption-molecular aggregation" significantly suppressed the translational motion of asphaltenes.

3.4. QSAR model for diffusion coefficients

The diffusion coefficients of various oil molecules within distinct regions of the kerogen matrix were systematically calculated to elucidate the intrinsic correlation between molecular migration behavior and structural attributes. The selected representative molecules encompassed light hydrocarbons (hexane, heptane, octane, nonane, cyclohexane, cycloheptane, benzene,

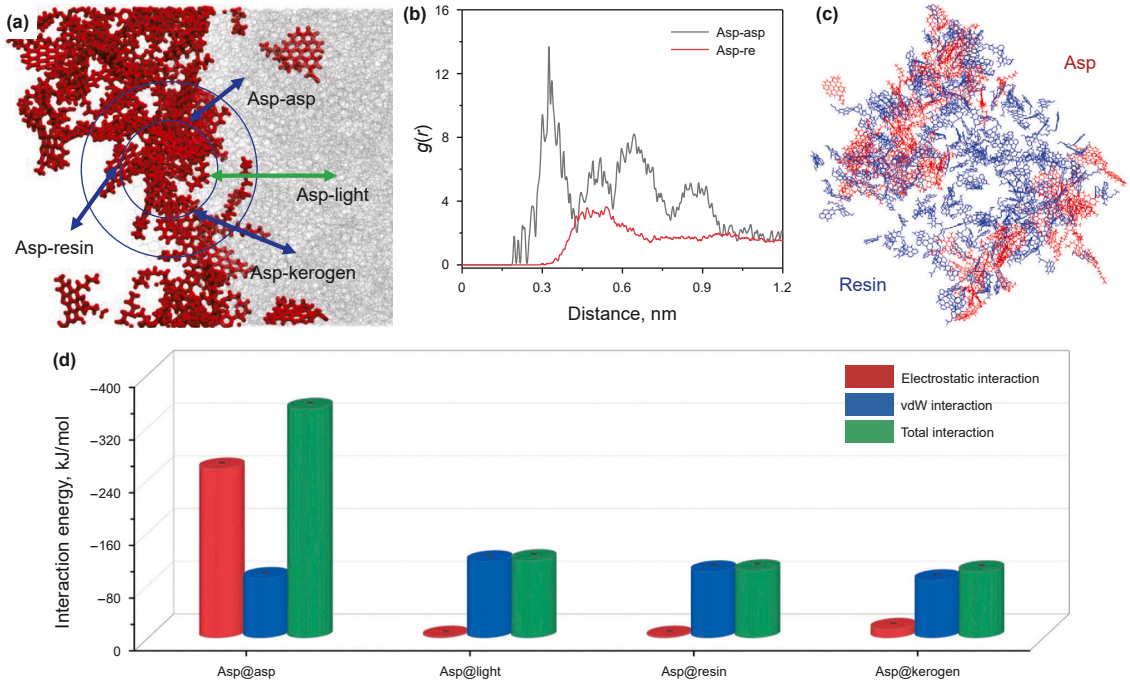


Fig. 7. **(a)** Schematic illustration of the interactions between an asphaltene molecule and surrounding molecules. **(b)** Radial distribution functions (RDF) between asphaltene-asphaltene molecules and between asphaltene-resin molecules. **(c)** Snapshot illustrating the interactions between asphaltene and resin molecules. **(d)** Interaction energies between the asphaltene molecule and surrounding molecules.

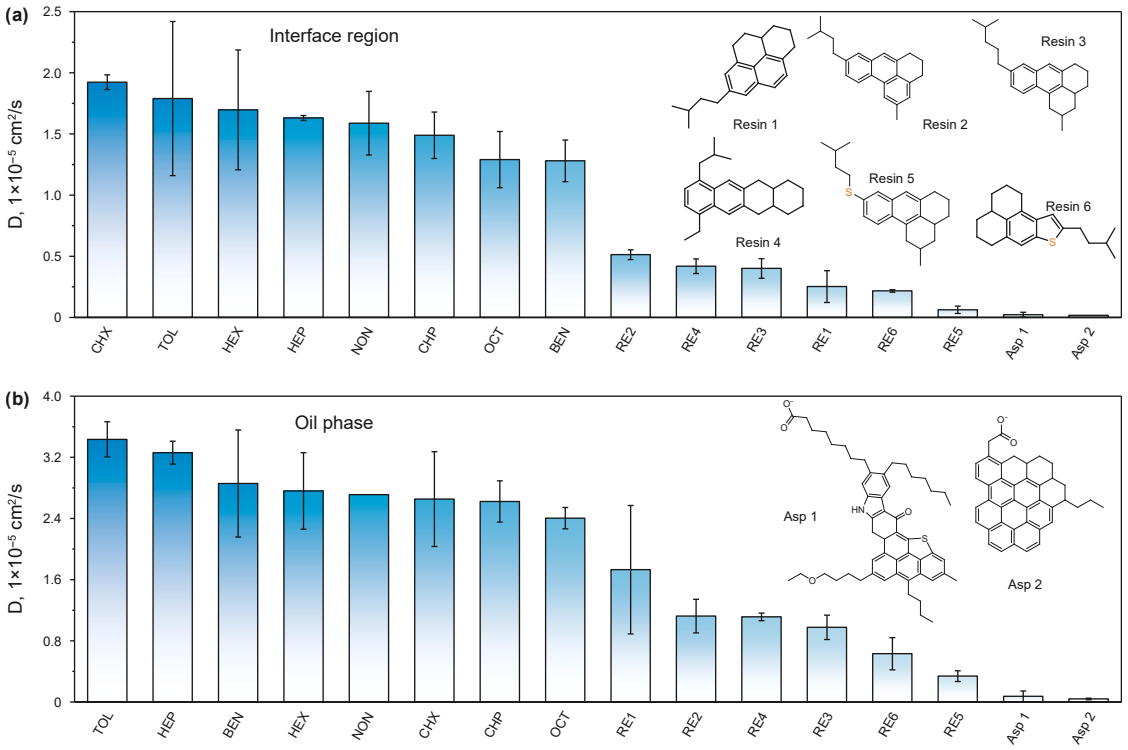


Fig. 8. Diffusion coefficients of different oil molecules in **(a)** interface region, and **(b)** oil phase.

toluene), structurally diverse resin molecules (resin 1–resin 6), and asphaltenes (asphaltene 1 and asphaltene 2), thereby comprehensively reflecting the structural heterogeneity inherent to shale oil components.

Fig. 8(a) presented the distribution of diffusion coefficients for these molecules within the interface region. A distinct cascading trend was observed, with diffusion coefficients decreasing in a stepwise manner from light oil (approximately 1.4–2.0 $\times$ 10^{-5} cm^2/s) to resins (0.2–0.5 $\times$ 10^{-5} cm^2/s), and finally to asphaltenes. This hierarchy indicated that molecular weight and structural complexity were the critical determinants constraining diffusion capacity. Specifically, light hydrocarbon molecules, characterized by lower molecular weights and simpler configurations, exhibited higher degrees of motional freedom, whereas the high-molecular-weight, highly aromatic asphaltenes suffered the most severe diffusion suppression. Furthermore, a comparative analysis of resin molecules with similar molecular weights revealed that Resin 5 and Resin 6, which possessed higher heteroatom contents, displayed significantly lower diffusion coefficients than their counterparts. This suggested that the introduction of heteroatoms potentiated non-bonded interactions (intermolecularly and between the molecules and the kerogen matrix), thereby further retarding their migratory capability. Fig. 8(b) illustrated the diffusion coefficients within the oil phase region. Similar to the interface region, the diffusion rates adhered to the fundamental order of asphaltenes < resins (about 0.8 $\times$ 10^{-5} cm^2/s) < light oil (about 2.8 $\times$ 10^{-5} cm^2/s), demonstrating the universality of the dominant influence exerted by intrinsic molecular structural features on transport behavior. However, compared to the interface region, the diffusion coefficients for all molecules in the oil phase increased significantly, reflecting the regulatory impact of the chemical environment on migration dynamics. Within the oil phase, the attenuation of molecule-kerogen interactions and the reduction of spatial confinement allowed the oil molecules to exhibit diffusion characteristics that more closely approximated those of bulk fluids. Collectively, these results demonstrated that the diffusion behavior of oil molecules within kerogen nanopores was the outcome of a concerted interplay between intrinsic molecular attributes (e.g., molecular weight, aromaticity, and heteroatom content) and the local chemical environment (interface vs. oil phase). The intensified molecule—solid interactions in the interface region significantly inhibited diffusion, whereas the oil phase provided relatively favorable conditions for migration.

To quantitatively elucidate the structure-activity relationship between the diffusion behavior of oil molecules in kerogen nanopores and their intrinsic molecular attributes, QSAR model was constructed utilizing the diffusion coefficients of 16 representative molecules within the oil phase region (Fig. 8(b)). Data from the oil phase region were specifically selected to mitigate the confounding effects of kerogen pore wall and interfacial constraints, thereby isolating the dominant influence of molecular structure and physicochemical properties on transport behavior. Drawing upon previous research, 17 molecular descriptors were initially introduced to comprehensively delineate the structural features of the various oil components (Yuan et al., 2024a). These molecular descriptors were characterized molecular mass, electronic distribution, and surface properties. Subsequently, a systematic screening of these descriptors was performed via correlation analysis. The correlation coefficients between the diffusion coefficients and individual descriptors are presented in Fig. 9(b), while the inter-descriptor correlation matrix is displayed in Fig. 9(a). The selection process adhered to two fundamental principles: first, descriptors were required to exhibit significant correlation with the diffusion coefficient to ensure a clear physical indication of transport behavior; and second, high multicollinearity between descriptors was avoided to enhance the robustness and interpretability of the model. Following this stepwise refinement, six key descriptors were retained: total molecular mass, σ^2_{tot}, positive surface area of ESP, nonpolar surface area, maximal value of ESP, and positive average

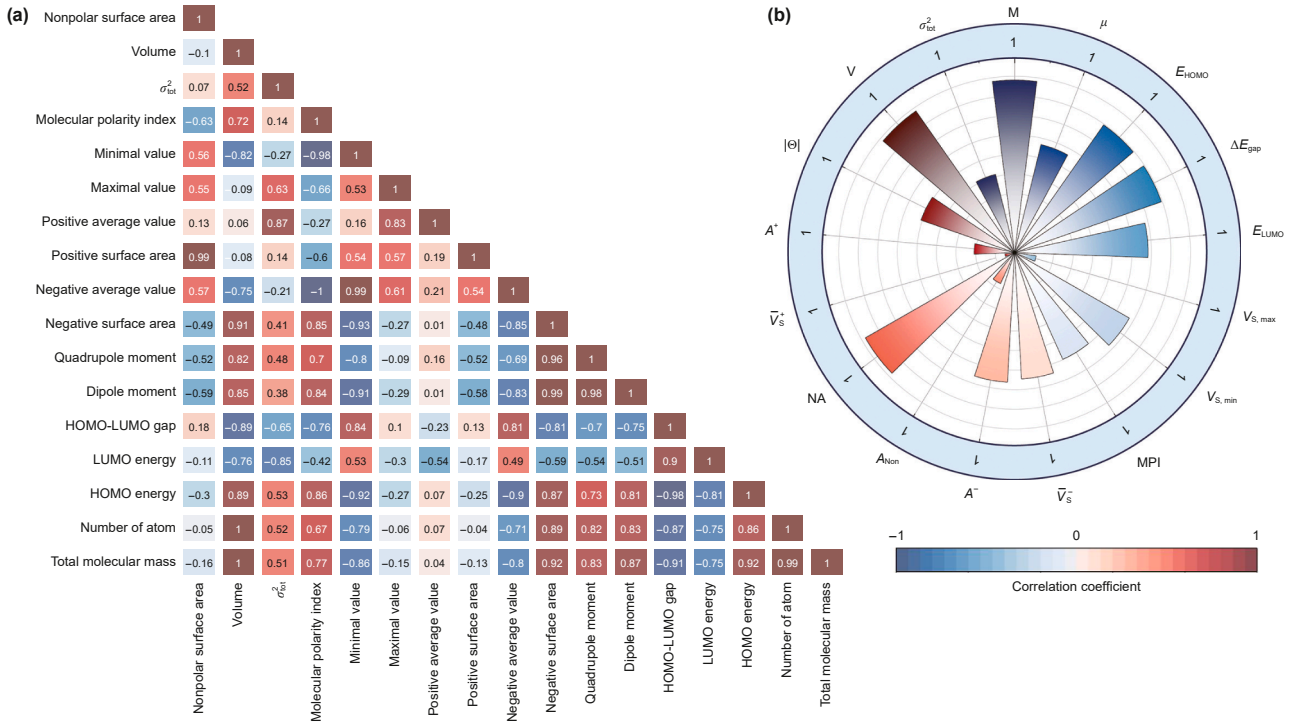


Fig. 9. **(a)** Correlation coefficient matrix among the selected molecular descriptors. **(b)** Correlation analysis between the diffusion coefficients and the selected molecular descriptors.

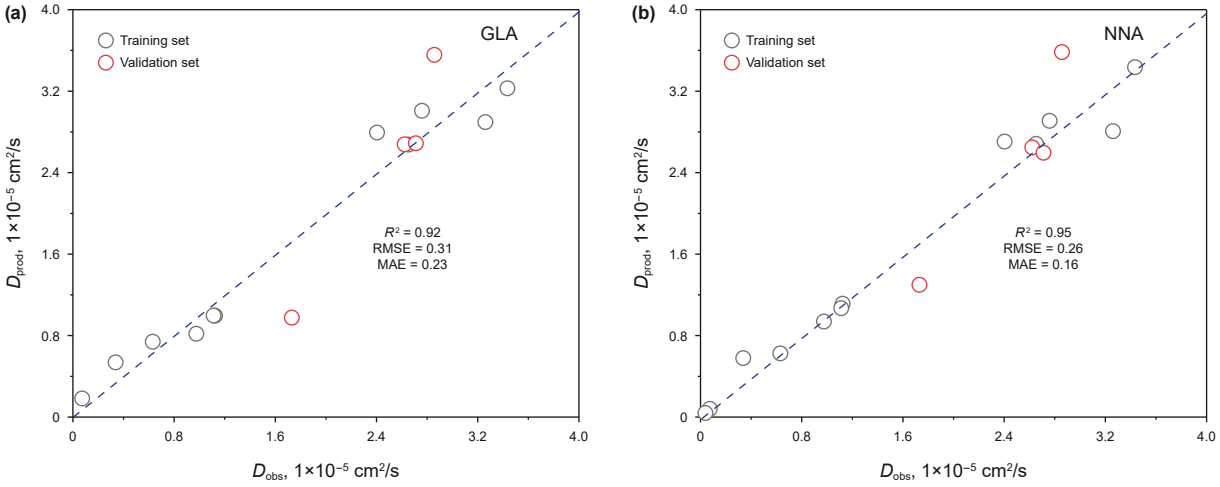


Fig. 10. Comparison of the observed and predicted diffusion coefficients for validation and training data sets by QSAR **(a)** GFA model and **(b)** NNA model.

value of ESP. These descriptors collectively reflect molecular size, polarity, and electrostatic potential distribution characteristics at the molecular scale, providing a rational framework for characterizing disparities in diffusivity. Then, GFA and NNA models were constructed, and their performances were systematically evaluated in Fig. 10(a) and (b). The results indicated that the NNA model possessed a distinct advantage in capturing the non-linear relationships between diffusion coefficients and multi-dimensional molecular descriptors. Its predictive accuracy significantly outperformed that of the GFA model, as evidenced by higher coefficients of determination and lower error metrics ($R^2 = 0.95$, RMSE = 0.26, MAE = 0.16). This finding suggested that the diffusion behavior of oil molecules in kerogen pores is synergistically governed by multiple molecular attributes, characterized by pronounced non-linear structure-activity relationships. The developed QSAR model quantitatively identifies molecular features that govern oil diffusivity in kerogen nanopores, indicating that lighter, less polar molecules with lower electrostatic heterogeneity exhibit higher transport mobility. These results provide practical criteria for assessing the producibility of different oil fractions and for selecting or tailoring stimulation strategies, such as thermal or solvent-based treatments, to preferentially mobilize low-diffusivity components. The model further enables rapid screening of molecular diffusivity, supporting data-driven optimization of shale oil recovery processes.

4. Conclusions

In summary, this research established a comprehensive molecular-scale framework to quantify the partitioning and transport mechanisms of shale oil within kerogen nanopores. The investigation demonstrated that the pore volume is partitioned into distinct thermodynamic zones, where a 7.49 nm interface region serves as a critical entrapment zone for heavy components. A key finding was the disproportionate interfacial occupancy of asphaltenes, which exhibited a contact frequency nearly ten-fold higher than that of light hydrocarbons. This disparity is fundamentally rooted in a "dual-inhibition" mechanism: the strong adsorption potential of the kerogen wall coupled with the high propensity of asphaltenes for self-aggregation through π-π stacking. Such interactions effectively anchor heavy molecules near the pore surface, reducing their motion to localized vibrations and creating a stagnant layer that impedes overall fluid mobility. Furthermore, the integration of machine learning confirmed that molecular diffusivity in these confined environments is a complex, non-linear function of intrinsic structural descriptors, with the NNA model providing superior predictive reliability. This suggests that the transport hierarchy (light oil > resins > asphaltenes) remains consistent across different pore regions, though the absolute magnitudes are modulated by the local chemical environment. The transport of shale oil is a multiscale phenomenon governed by the intricate interplay between pore geometry and mineralogy. Previous studies have demonstrated that while circular pore models are common, actual shale matrices contain complex slit-like and angular pores that can enhance transport capacity by over 100% (Yu et al. 2019, 2023). Furthermore, the coexistence of organic kerogen and inorganic minerals introduces a competition between viscous flow and surface diffusion, where the transport mechanism is highly sensitive to both pore width and reservoir pressure (Yu et al. 2018, 2020). By integrating these perspectives, it becomes evident that the "wall adsorption-molecular aggregation" mechanism identified in our kerogen model represents the primary bottleneck within the organic domains, while inorganic matter may provide alternative pathways with distinct boundary conditions.

To bridge the gap between molecular-scale insights and reservoir-scale applications, future research should focus on hierarchical upscaling frameworks that integrate molecular dynamics with pore-scale and continuum-scale models. The transport coefficients and "dual-inhibition" mechanisms identified in this study can serve as critical constitutive parameters for Lattice Boltzmann Method (LBM) or Pore Network Modeling (PNM) to accurately capture the evolution of apparent permeability in complex porous matrices (Yu et al., 2021). Furthermore, incorporating these fluid-solid interaction disparities into a quadruple-domain Finite Element Method (FEM) approach would allow for a more comprehensive analysis of how hydraulic fracture propagation and matrix deformation synergistically influence the recovery of diverse oil fractions (Yu et al., 2023). By focusing on a 10 nm model, we provide a median scenario that captures the essential physics of both hindered and free transport states. To account for the broader implications of particle size distribution in future iterations, our results can be integrated into PNM or stochastic continuum models as a size-dependent boundary condition.

CRediT authorship contribution statement

Shi-Deng Yuan: Writing – review & editing, Writing – original draft, Methodology, Investigation, Funding acquisition, Formal analysis, Data curation, Conceptualization. **Ji-Chao Fang:** Writing – review & editing, Writing – original draft, Methodology, Investigation, Funding acquisition.

Declaration of competing interest

The authors declare that they have no known competing financial interests or personal relationships that could have appeared to influence the work reported in this paper.

Acknowledgments

This work was financially supported by the Shandong Provincial University Youth Innovation Science and Technology Support Program (2025KJH165), the National Natural Science Foundation of China (52204069), and the Natural Science Foundation of Shandong Province (ZR2024QB118).

Supplementary data

Supplementary data to this article can be found online at https://doi.org/10.1016/j.petsci.2026.05.007.

References

Allen, M.P., Tildesley, D.J., 1987. Computer Simulation of Liquids. Clarendon Press Oxford.
Bousige, C., Ghimbeu, C.M., Vix-Guterl, C., et al., 2016. Realistic molecular model of kerogen's nanostructure. Nat. Mater. 15 (5), 576–582. https://doi.org/10.1038/nmat4541.
Bui, K., Akkutlu, I.Y., Silas, J.A., 2020. Mass and momentum transfer considerations for oil displacement in source rocks using microemulsion solutions. Fluid 5 (2), 44. https://doi.org/10.3390/fluids5020044.
Chen, F., Tang, J., Wang, J., 2023. Effects of π–π stacking on shale gas adsorption and transport in nanopores. ACS Omega 8 (49), 46577–46588. https://doi.org/10.1021/acsomega.3c05522.
Chen, S., Huang, Z., Zhu, G., et al., 2026. Experimental techniques for qualitative and quantitative characterization of shale oil reservoir space, minerals, and fluids. Energy Geosci. 7 (2), 100516. https://doi.org/10.1016/j.engeos.2025.100516.
Chiang, W.-S., Chen, J.-H., Jacobi, D., et al., 2020. Structural properties of kerogens with different maturities. Energy Fuels 34 (10), 12354–12365. https://doi.org/10.1021/acs.energyfuels.0c02268.
Clarkson, C.R., Solano, N., Bustin, R.M., et al., 2013. Pore structure characterization of North American shale gas reservoirs using USANS/SANS, gas adsorption, and mercury intrusion. Fuel 103, 606–616. https://doi.org/10.1016/j.fuel.2012.06.119.
Cui, P., Yuan, S., Zhang, X., et al., 2026. Aging-induced changes in the molecular structure and interactions of pavement asphalt. Comput. Theor. Chem. 1255, 115579. https://doi.org/10.1016/j.comptc.2025.115579.
Dawass, N., Vasileiadis, M., Peristeras, L.D., Papavasileiou, K.D., Economou, I.G., 2023. Prediction of adsorption and diffusion of shale gas in composite pores consisting of kaolinite and kerogen using molecular simulation. J. Phys. Chem. C 127 (20), 9452–9462. https://doi.org/10.1021/acs.jpcc.3c00499.
Fei, J., Wang, M., Li, J., Zhao, C., Wang, X., Zhang, L., Yu, C., Li, Y., Dong, S., 2023. Molecular dynamics simulation of adsorption and absorption behavior of shale oil in realistic kerogen slits. Energy Fuels 37 (5), 3654–3671. https://doi.org/10.1021/acs.energyfuels.2c03842.
Feng, Q., Xu, S., Xing, X., Zhang, W., Wang, S., 2020. Advances and challenges in shale oil development: a critical review. Adv. Geo-Energy Res. 4 (4), 406–418. https://doi.org/10.46690/ager.2020.04.06.
Gao, Z., Fan, Y., Xuan, Q., Zheng, G., 2020. A review of shale pore structure evolution characteristics with increasing thermal maturities. Adv. Geo-Energy Res. 4 (3), 247–259. https://doi.org/10.46690/ager.2020.03.03.
Gong, H., Zhu, C., Zhang, Y., Li, Z., San, Q., Xu, L., Li, Y., Dong, M., Hassanzadeh, H., 2020. Experimental evaluation on the oil saturation and movability in the organic and inorganic matter of shale. Energy Fuels 34 (7), 8063–8073. https://doi.org/10.1021/acs.energyfuels.0c00831.
Grimme, S., 2008. Do special noncovalent π–π stacking interactions really exist? Angew. Chem. Int. Ed. 47 (18), 3430–3434. https://doi.org/10.1002/anie.200705157.
Li, Y., Yao, J., Sun, H., Yang, Y., Zhong, J., 2025. Phase behavior and critical properties of long-chain alkane confined in shale nanopores: a gauge-gibbs monte carlo simulations study. Langmuir 41 (51), 34395–34411. https://doi.org/10.1021/acs.langmuir.5c04740.
Lin, X., Li, Z., Jiang, Z., He, T., Jiang, Z., Qin, C., Zhang, C., 2023. Simulation of methane occurrence in rough nanokerogen slits. Energy Fuels 37 (20), 15476–15489. https://doi.org/10.1021/acs.energyfuels.3c02110.

Liu, X., Zhang, D., 2019. A review of phase behavior simulation of hydrocarbons in confined space: implications for shale oil and shale gas. J. Nat. Gas Sci. Eng. 68, 102901. https://doi.org/10.1016/j.jngse.2019.102901.
Lu, T., 2024. A comprehensive electron wavefunction analysis toolbox for chemists, Multiwfn. J. Chem. Phys. 161 (8), 082503. https://doi.org/10.1063/5.0216272.
Lu, T., Chen, F., 2012. Multiwfn: a multifunctional wavefunction analyzer. J. Comput. Chem. 33 (5), 580–592. https://doi.org/10.1002/jcc.22885.
Lu, T., Chen, Q., 2022. Independent gradient model based on Hirshfeld partition: a new method for visual study of interactions in chemical systems. J. Comput. Chem. 43 (8), 539–555. https://doi.org/10.1002/jcc.26812.
Mehana, M., Kang, Q., Nasrabadi, H., Viswanathan, H., 2021. Molecular modeling of subsurface phenomena related to petroleum engineering. Energy Fuels 35 (4), 2851–2869. https://doi.org/10.1021/acs.energyfuels.0c02961.
Michalec, L., Lísal, M., 2017. Molecular simulation of shale gas adsorption onto overmature type II model kerogen with control microporosity. Mol. Phys. 115 (9–12), 1086–1103. https://doi.org/10.1080/00268976.2016.1243739.
Nadeau, P.H., Sun, S., Ehrenberg, S.N., 2023. The “Golden zone” temperature distribution of oil and gas occurrence examined using a global empirical database. Mar. Petrol. Geol. 158, 106507. https://doi.org/10.1016/j.marpetgeo.2023.106507.
Neese, F., 2022. Software update: the ORCA program system—version 5.0. WIREs Comput. Mol. Sci. 12 (5), e1606. https://doi.org/10.1002/wcms.1606.
Okiongbo, K.S., Aplin, A.C., Larter, S.R., 2005. Changes in type II kerogen density as a function of maturity: evidence from the Kimmeridge Clay Formation. Energy Fuels 19 (6), 2495–2499. https://doi.org/10.1021/ef050194+.
Perez, F., Devegowda, D., 2019. Spatial distribution of reservoir fluids in mature kerogen using molecular simulations. Fuel 235, 448–459. https://doi.org/10.1016/j.fuel.2018.08.024.
Ross, D.J.K., Marc Bustin, R., 2009. The importance of shale composition and pore structure upon gas storage potential of shale gas reservoirs. Mar. Petrol. Geol. 26 (6), 916–927. https://doi.org/10.1016/j.marpetgeo.2008.06.004.
Sang, Q., Zhang, S., Li, Y., Dong, M., Bryant, S., 2018. Determination of organic and inorganic hydrocarbon saturations and effective porosities in shale using vacuum-imbibition method. Int. J. Coal Geol. 200, 123–134. https://doi.org/10.1016/j.coal.2018.10.010.
Schuler, B., Zhang, Y., Liu, F., Pomerantz, A.E., Andrews, A.B., Gross, L., Pauchard, V., Banerjee, S., Mullins, O.C., 2020. Overview of asphaltene nanostructures and thermodynamic applications. Energy Fuels 34 (12), 15082–15105. https://doi.org/10.1021/acs.energyfuels.0c00874.
Stephens, P.J., Devlin, F.J., Chabalowski, C.F., Frisch, M.J., 1994. Ab initio calculation of vibrational absorption and circular dichroism spectra using density functional force fields. J. Phys. Chem. 98 (45), 11623–11627. https://doi.org/10.1021/j100096a001.
Ungerer, P., Collell, J., Yiannourakou, M., 2015. Molecular modeling of the volumetric and thermodynamic properties of kerogen: influence of organic type and maturity. Energy Fuels 29 (1), 91–105. https://doi.org/10.1021/ef502154k.
Vasileiadis, M., Peristeras, L.D., Papavasileiou, K.D., Economou, I.G., 2018. Transport properties of shale gas in relation to kerogen porosity. J. Phys. Chem. C 122 (11), 6166–6177. https://doi.org/10.1021/acs.jpcc.8b00162.
Wang, B., Yang, K., Bai, B., Liu, F., Liu, J., Gao, Q., Xu, X., 2025. Unraveling mechanisms of CO_2-regulated pyridine adsorption on kerogen: quantum chemistry insights for advancing CO_2-enhanced shale oil recovery. Chem. Eng. J. 519, 165076. https://doi.org/10.1016/j.cej.2025.165076.
Wang, Y., Han, X., Li, J., Liu, R., Wang, Q., Huang, C., Wang, X., Zhang, L., Lin, R., 2023. Review on oil displacement technologies of enhanced oil recovery: state-of-the-art and outlook. Energy Fuels 37 (4), 2539–2568. https://doi.org/10.1021/acs.energyfuels.2c03625.
Wu, H., Wen, L., Zhang, L., Wang, D., Li, N., Yang, M., 2022. Gas adsorption capacity of Type-II Kerogen at a varying burial depth. Energy Fuels 36 (14), 7472–7482. https://doi.org/10.1021/acs.energyfuels.2c01176.
Xie, C., Huang, J., Jiang, S., Zhao, H., Wu, Z., 2024. Effect of water content and salinity on CH_4/CO_2 competitive adsorption in organic and clay nanopores: a molecular perspective. Energy Fuels 38 (24), 23507–23518. https://doi.org/10.1021/acs.energyfuels.4c04744.
Xu, Y., Lun, Z., Pan, Z., Wang, H., Zhou, X., Zhao, C., Zhang, D., 2022. Occurrence space and state of shale oil: a review. J. Petrol. Sci. Eng. 211, 110183. https://doi.org/10.1016/j.petrol.2022.110183.
Yang, J., Hatcherian, J., Hackley, P.C., Pomerantz, A.E., 2017. Nanoscale geochemical and geomechanical characterization of organic matter in shale. Nat. Commun. 8 (1), 2179. https://doi.org/10.1038/s41467-017-02254-0.
Yang, X., Chen, J., Zhang, X., Jiang, F., Pang, H., 2025a. Influence of the mineral composition and pore structure on the tensile mechanical properties of shale from a microscopic perspective: insights from molecular dynamics simulations. Int. J. Rock Mech. Min. Sci. 191, 106123. https://doi.org/10.1016/j.ijrmms.2025.106123.
Yang, X., Shen, H., Fang, G., Ma, Q., Cheng, S., Yang, J., 2025b. Practical molecular reconstruction method for heavy oil based on SARA fractions simulated blending. Chem. Eng. J. 508, 161050. https://doi.org/10.1016/j.cej.2025.161050.
Yang, Y., Liu, J., Yao, J., Kou, J., Li, Z., Wu, T., Zhang, K., Zhang, L., Sun, H., 2020. Adsorption behaviors of shale oil in kerogen slit by molecular simulation. Chem. Eng. J. 387, 124054. https://doi.org/10.1016/j.cej.2020.124054.
Yu, H., Fan, J., Chen, J., Zhu, Y., Wu, H., 2018. Pressure-dependent transport characteristic of methane gas in slit nanopores. Int. J. Heat Mass Tran. 123, 657–667. https://doi.org/10.1016/j.ijheatmasstransfer.2018.03.003.
Yu, H., Xu, H., Fan, J., Wang, F., Wu, H., 2020. Roughness factor-dependent transport characteristic of shale gas through amorphous kerogen nanopores. J. Phys. Chem. C 124 (23), 12752–12765. https://doi.org/10.1021/acs.jpcc.0c02456.
Yu, H., Xu, H., Fan, J., Zhu, Y.-B., Wang, F., Wu, H., 2021. Transport of shale gas in microporous/nanoporous media: molecular to pore-scale simulations. Energy Fuels 35 (2), 911–943. https://doi.org/10.1021/acs.energyfuels.0c03276.
Yu, H., Xu, W., Li, B., Huang, H., Micheal, M., Wang, Q., Huang, M., Meng, S., Liu, H., Wu, H., 2023. Hydraulic fracturing and enhanced recovery in shale reservoirs: theoretical analysis to engineering applications. Energy Fuels 37 (14), 9956–9997. https://doi.org/10.1021/acs.energyfuels.3c01029.
Yu, H., Zhu, Y., Jin, X., Liu, H., Wu, H., 2019. Multiscale simulations of shale gas transport in micro/nano-porous shale matrix considering pore structure influence. J. Nat. Gas Sci. Eng. 64, 28–40. https://doi.org/10.1016/j.jngse.2019.01.016.
Yuan, S., Wang, H., Du, Q., Fang, J., 2026a. Mechanistic insights into heat-induced demulsification of oil/water emulsions driven by surfactant type. Colloids Surf. A Physicochem. Eng. Asp. 728, 138489. https://doi.org/10.1016/j.colsurfa.2025.138489.
Yuan, S., Wang, L., Liu, S., Cao, X., 2025a. Molecular dynamics insights into oil droplet adsorption and penetration on the stratum corneum. Langmuir 41 (47), 31890–31899. https://doi.org/10.1021/acs.langmuir.5c04028.
Yuan, S., Wang, L., Zhang, X., Cao, X., Yuan, S., 2026b. Molecular structure-dependent interfacial behavior of asphaltenes at the oil-water interface. Colloids Surf. A Physicochem. Eng. Asp. 733, 139296. https://doi.org/10.1016/j.colsurfa.2025.139296.
Yuan, S., Yang, X., Zhang, N., Zhang, J., Yuan, S., Wang, Z., 2024a. Molecular insights into the adsorption and penetration of oil droplets on hydrophobic membrane in membrane distillation. Water Res. 253, 121329. https://doi.org/10.1016/j.watres.2024.121329.
Yuan, S., Zhang, J., Yu, X., Zhu, X., Zhang, N., Yuan, S., Wang, Z., 2025b. Molecular mechanisms of humic acid in inhibiting silica scaling during membrane distillation. Environ. Sci. Technol. 59 (1), 978–988. https://doi.org/10.1021/acs.est.4c10047.
Yuan, S., Zhang, N., Yuan, S., Wang, Z., 2024b. Insights into the silica scaling behaviors in membrane distillation and anti-scaling mechanism of functional polymers. Water Res. 261, 122006. https://doi.org/10.1016/j.watres.2024.122006.
Zhan, S., Bao, J., Wang, X., Wang, W., Su, Y., Zhang, M., Wang, Y., Jin, Z., 2024. A comparative study of shale oil transport behavior in graphene and kerogen nanopores with various roughness via molecular dynamics simulations. Chem. Eng. J. 498, 155173. https://doi.org/10.1016/j.cej.2024.155173.
Zhang, A., Lu, Y., 2025. Confined transport property of multi-polar mixed shale oil components induced by interfacial effects within kerogen nanopores. Fuel 393, 134985. https://doi.org/10.1016/j.fuel.2025.134985.
Zhang, J., Lu, T., 2021. Efficient evaluation of electrostatic potential with computerized optimized code. Phys. Chem. Chem. Phys. 23 (36), 20323–20328. https://doi.org/10.1039/D1CP02805G.
Zhang, Y., He, K., Wang, X., Zhang, X., Liu, X., Lu, X., 2025a. Adsorption and diffusion of shale gas in kerogen matrix: insights from molecular simulations. Fuel 386, 134246. https://doi.org/10.1016/j.fuel.2024.134246.
Zhang, Y., Jiang, Y., Zhang, J., Huang, H., Wang, T., Wang, J., Ren, Y., Cui, X., 2025b. Mechanism of enhanced oil recovery via carbon dioxide flooding in kerogen nanopores: a molecular dynamics approach. Fuel 390, 134626. https://doi.org/10.1016/j.fuel.2025.134626.
Zhao, S., Tang, X., Pu, W., He, M., Yang, Y., 2024. Kinetic modeling for upgrading of heavy crude oil via thermal cracking in porous media: SARA fractions and gas compositions. Fuel 371, 132087. https://doi.org/10.1016/j.fuel.2024.132087.
Zhao, Y., Guan, B., Zhang, T., Ge, F., Yang, X., Hu, H., Thanh, H.V., Zuo, H., Zhang, L., 2025. CO_2 and H_2 behavior in kerogen matrix with CH_4 presence: molecular insights and implications. J. Mol. Liq. 437, 128453. https://doi.org/10.1016/j.molliq.2025.128453.
Zhu, C., Sheng, J.J., Ettehadtavakkol, A., Li, Y., Dong, M., 2020. Numerical and experimental study of oil transfer in laminated shale. Int. J. Coal Geol. 217, 103365. https://doi.org/10.1016/j.coal.2019.103365.